Short communication

Facile synthesis of hierarchical Co$_3$O$_4$@MnO$_2$ core–shell arrays on Ni foam for asymmetric supercapacitors

Ming Huang [a], Yuxin Zhang [a,b,*], Fei Li [a], Lili Zhang [c,**], Zhiyu Wen [b], Qing Liu [a,**]

[a] College of Material Science and Engineering, Chongqing University, Chongqing 400044, PR China
[b] National Key Laboratory of Fundamental Science of Micro/Nano-Devices and System Technology, Chongqing University, Chongqing 400044, PR China
[c] Institute of Chemical and Engineering Sciences, A*STAR, 1 Pesek Road, Jurong Island, 627833 Singapore, Singapore

HIGHLIGHTS

- Hierarchical Co$_3$O$_4$@MnO$_2$ nanowire array was prepared by a facile hydrothermal method.
- MnO$_2$ coated on Co$_3$O$_4$ nanowire without carbon coating or electrochemical deposition.
- The unique core–shell architecture exhibits a high capacitance of 560 F g^{-1}.
- Excellent cycling stability: 95% capacitance retention after 5000 cycles.
- The asymmetric supercapacitor yielded a maximum power density of 158 kW kg^{-1}.

GRAPHICAL ABSTRACT
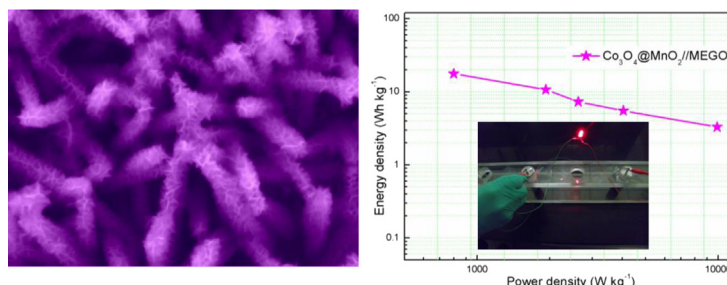
ARTICLE INFO

ABSTRACT

Hierarchical Co$_3$O$_4$@MnO$_2$ core–shell arrays on Ni foam have been fabricated by a facile hydrothermal approach and further investigated as the electrode for high-performance supercapacitors. Owing to the high conductivity of the well-defined mesoporous Co$_3$O$_4$ nanowire arrays in combination with the large surface area provided by the ultrathin MnO$_2$ nanosheets, the unique designed Co$_3$O$_4$@MnO$_2$ core–shell arrays on Ni foam have exhibited a high specific capacitance (560 F g^{-1} at a current density of 0.2 A g^{-1}), good rate capability, and excellent cycling stability (95% capacitance retention after 5000 cycles). An asymmetric supercapacitor with Co$_3$O$_4$@MnO$_2$ core–shell nanostructure as the positive electrode and activated microwave exfoliated graphite oxide activated graphene (MEGO) as the negative electrode yielded an energy density of 17.7 Wh kg^{-1} and a maximum power density of 158 kW kg^{-1}. The rational design of the unique core–shell array architectures demonstrated in this work provides a new and facile approach to fabricate high-performance electrode for supercapacitors.

© 2013 Elsevier B.V. All rights reserved.

1. Introduction

The increasing demand for sustainable and renewable power sources in modern electronic industries has stimulated intensive research efforts on the developments of high-performance, lightweight and environmental friendly energy storage devices [1–3]. Among various emerging energy storage technologies,

* Corresponding author. College of Material Science and Engineering, Chongqing University, Chongqing 400044, PR China. Tel./fax: +86 2365104131.
** Corresponding authors.
E-mail addresses: zhangyuxin@cqu.edu.cn (Y. Zhang), zhang_lili@ices.a-star.edu.sg (L. Zhang), qingliu@cqu.edu.cn (Q. Liu).

supercapacitors (SCs), also known as electrochemical capacitors (ECs), are the ideal candidates for green energy storage because of their high power density, excellent pulse charge–discharge characteristics, super-high cycling life and safe operation [4–6]. Based on the mechanism of charge storage, supercapacitors can be classified as two kinds: electrical double-layer capacitors (EDLCs) that typically use carbon-active materials and pseudocapacitors that use redox-active materials [7,8]. In particular, pseudocapacitors based on the transition metal oxides/hydroxides with variable valence exhibit a higher specific capacitance than those based on carbonaceous materials and conducting polymers as they can provide a variety of oxidation states for efficient redox charge transfer [9–12]. Therefore, great efforts have been devoted to searching for inexpensive transition metal oxides with good capacitive characteristics, such as Co_3O_4 [13], NiO [14], MnO_2 [15], Fe_2O_3 [16], V_2O_5 [17], and CuO [18].

Among these candidate materials, MnO_2 exhibits many intriguing characteristics, such as low cost, environmental friendliness, natural abundance, high theoretical capacity (1370 F g^{-1}), and wide operating potential window, suggesting it as the most promising electrode material for supercapacitors. However, low surface areas and poor electrical conductivity (10^{-5}–10^{-6} S cm^{-1}) of MnO_2 limits the charge–discharge rate for high-performance supercapacitors [19–21]. In this regard, further efforts are focused on incorporating MnO_2 nanostructures with carbon-based materials or conducting polymers [22–25]. By combing unique properties of individual constituents, improved rate capability and cycling ability could be achieved in such an electrode. Another problem of MnO_2-based materials arises from the low loading of active materials, which would lead to a low energy density. Therefore, it is still great challenge to boost the electrochemical utilization of the pseudocapacitance of MnO_2 by rationally designing MnO_2-based electrodes with novel structures and reliable electric connection. An emerging attractive concept is to directly grow smart integrated array architectures with the combination of multi-component structures on conducting substrates as binder-free electrodes for supercapacitors which can provide synergistic effects form all of their individual constituents, thus achieving high power and energy density, long cycle life, and high rate capability [26]. A challenge in this direction is to develop a desirable smart architecture, in which electrochemical activities of each component are fully manifested and the kinetics of ion/electron transport are guaranteed. Based on the above consideration, various MnO_2-based nanocomposites with different geometrical attributes and morphological forms have been employed as electrodes for supercapacitors. For instance, $Co_3O_4@MnO_2$, $NiCo_2O_4@MnO_2$, $Zn_2SnO_4@MnO_2$, $Co_3O_4@Au@MnO_2$, $Co_3O_4@Pt@MnO_2$, $TiO_2@MnO_2$, and $Fe_2O_3@MnO_2$ nanocomposites have been developed with improved electrochemical performance [27–34]. However, the synthetic procedures for these unique MnO_2-based core–shell structures are still relatively complicated since they either need carbon coating or electrochemical deposition process. Thus, a novel but simple design and fabrication of multi-component hierarchical heterostructures with highly-accessible surface areas and fast ion diffusion for supercapacitors still remains a challenge.

Herein, we demonstrate a facile and cost-effective approach to design and fabricate hierarchical $Co_3O_4@MnO_2$ core–shell arrays on Ni foam as a binder-free electrode for high-performance supercapacitors, in which the mesoporous Co_3O_4 arrays served as the "core" and the ultrathin branch MnO_2 nanosheets are the "shell" layer. By virtue of the synergetic contribution from individual constituents and the sophisticated configuration, the resulting $Co_3O_4@MnO_2$ core–shell arrays exhibit a much higher capacitance (560 F g^{-1}) and excellent cycling ability (95% retention after 5000 cycles) with respect to pristine Co_3O_4 arrays. In addition,

an asymmetric supercapacitor with hierarchical $Co_3O_4@MnO_2$ core–shell arrays as the positive electrode and activated microwave exfoliated graphite oxide activated graphene (MEGO) as the negative electrode manifests an energy density of 17.7 Wh kg^{-1} with a maximum power density of 158 kW kg^{-1}. Undoubtedly, the facile design of hierarchical architecture and control over the multi-composition demonstrated in this work offers a promising strategy for the fabrication of high-performance electrodes for supercapacitors.

2. Experimental

2.1. Materials

All the chemical reagents were purchased from Alfa Aesar, which were of analytical purity and used without any further purification.

2.2. Synthesis of Co_3O_4 nanowire arrays

The Co_3O_4 nanowire arrays were fabricated by a modified hydrothermal method according to the previous work [35]. In a typical synthesis, $Co(NO_3)_2·6H_2O$ (1–4 mmol), NH_4F (2–8 mmol), $CO(NH_2)_2$ (5–20 mmol) were dissolved in 50 mL of deionized water and stirred for 10 min to form a clear solution (the different mixture solutions were used to obtain different morphologies of Co_3O_4 arrays). Nickel foam (1 × 2 cm^2) was carefully cleaned with 3 M HCl solution in an ultrasound bath for 5 min to remove the surface NiO layer, and then cleaned with deionized water and ethanol for 5 min each. The aqueous solution and the Ni foam were transferred to a Teflon-lined stainless-steel autoclave and maintained at 105 °C for 5 h, and then cooled down to room temperature. The samples were rinsed several times with deionized water and ethanol with the assistance of ultrasonication, and dried at 80 °C for 8 h. Finally, the precursors were converted to Co_3O_4 by annealing in air at 350 °C for 2 h.

2.3. Synthesis of hierarchical $Co_3O_4@MnO_2$ core–shell arrays

The hierarchical $Co_3O_4@MnO_2$ core–shell arrays were prepared using a facile hydrothermal method. Typically, the Co_3O_4 nanowire arrays on Ni foam was put into a Teflon-line stainless steel autoclave containing 30 mL $KMnO_4$ solution (0.015 M), which was subsequently maintained at 160 °C for 24 h. Finally, the samples were removed, washed with deionized water and ethanol, and dried at 60 °C to obtain hierarchical $Co_3O_4@MnO_2$ hybrid arrays. The mass of the as-grown MnO_2 materials was obtained by its weight differences before and after hydrothermal deposition.

2.4. Materials characterization

The crystallographic information and chemical composition of as-prepared products were established by powder X-ray diffraction (XRD, D/max 1200, Cu Kα). The morphological investigations of the Co_3O_4 arrays and $Co_3O_4@MnO_2$ core–shell arrays were carried out with focused ion beam (Zeiss Auriga FIB/SEM). Microstructures and energy-dispersive X-ray spectroscopy (EDS) were characterized by high-resolution transmission electron microscopy (HRTEM, Zeiss Libra 200). Nitrogen adsorption–desorption isotherms were measured at 77 K with micromeritics ASAP 2020 sorptometer. The specific surface area was calculated with the Brunauer–Emmett–Teller (BET) equation, and the pore size distributions were calculated from the adsorption curve by the Barrett–Joyner–Halenda (BJH) method.

2.5. Electrochemical measurements

A three-electrode system was used to measure the response of the Co₃O₄ nanowire arrays and hierarchical Co₃O₄@MnO₂ core—shell arrays with different morphologies as the working electrode using 1 M LiOH aqueous solution as the electrolyte, with a platinum plate as the counter electrode and saturated calomel electrode (SCE) as the reference electrode, respectively. The Ni foam supported nanostructures (1×1 cm²) acted directly as the working electrode.

The asymmetric supercapacitor was measured with a two-electrode system, including two slices of electrode material with the same size, a Whatman filter paper as separator, and 1 M LiOH solution as the electrolyte. In the two-electrode system, hierarchical Co₃O₄@MnO₂ core—shell arrays were the positive electrode, and activated microwave exfoliated graphite oxide activated graphene (MEGO) mixed with 20 wt% acetylene black and 10 wt% polyvinylidene fluoride (PVDF) in *N*-methyl-2-pyrrolidone (NMP) to form a paste and then pressed into uniform sheet was the negative electrode. The electrochemical performance in both three-electrode and two-electrode configurations was carried out on the CHI 660E electrochemical station. The cyclic voltammetry (CV) and galvanostatic charge—discharge techniques were employed to investigate the electrochemical performance of the electrodes. All the operating current densities were calculated based on the mass of active materials (mass of Co₃O₄@MnO₂ for three-electrode system and the total weight of Co₃O₄@MnO₂ with MEGO for two-electrode system). The electrochemical impedance spectroscopy (EIS) was conducted in the frequency range between 100 kHz and 0.01 Hz with a perturbation amplitude of 5 mV versus the open-circuit potential.

3. Results and discussion

3.1. Structure and morphology

Fig. 1 presents the composition and crystallite phase purity of the Co₃O₄ nanowire arrays and hierarchical Co₃O₄@MnO₂ core—shell arrays. As shown in Fig. 1a, except for the peaks originating from the Ni foam, the diffraction peaks of Co₃O₄ arrays are observed of 19.0°, 31.3°, 36.9°, 59.4°, and 65.2°, which could be assigned to the (111), (220), (311), (511), and (440) planes of the cubic Co₃O₄ (JCPDS card no. 42-1467). It can be observed in the XRD pattern of the hierarchical Co₃O₄@MnO₂ core—shell arrays that the diffraction peaks at about 12.5°, 25.2° and 37° are almost in accord with the standard XRD pattern of birnessite-type MnO₂ (JCPDS 80-1098),

indicating that the products are the mixture of Co₃O₄ and MnO₂ or Co₃O₄@MnO₂ core—shell nanostructures. Furthermore, the structure and phase purity of the MnO₂ samples obtained at the same condition as described in the Experimental section (hydrothermal reaction of 0.015 M KMnO₄ solution at 160 °C for 24 h) were examined by X-ray powder diffraction (see Supplementary information, SI-1). It can be seen that the typical peaks in our XRD pattern can be identified as birnessite-type MnO₂ (δ-MnO₂), which can be confirmed by the previous works [36—39].

As illustrated in Fig. 2a, the fabrication of hierarchical Co₃O₄@MnO₂ core—shell arrays on the Ni foam involved two steps. In the first step, Co₃O₄ nanowire arrays were grown on the Ni foam via a facile modified hydrothermal process. The second step was the deposition of a thin layer of MnO₂ nanosheets on the Co₃O₄ nanowire arrays via a hydrothermal deposition method, forming hierarchical Co₃O₄@MnO₂ core—shell arrays as the final product. Here, the deposition of MnO₂ nanosheets did not need the carbon layer coating or electrochemical deposition due to the fact that MnO₂ can be produced via self-decomposition of KMnO₄ during hydrothermal reaction. The morphologies of Co₃O₄ nanowires and the hierarchical Co₃O₄@MnO₂ core—shell arrays on Ni foam are investigated. Fig. 2b and c demonstrates the top-view SEM images of the Co₃O₄ nanowire arrays grown on Ni foam. Obviously, the slim Co₃O₄ nanowires with sharp tips are homogeneously aligned and separated apart adequately, forming a unique nanoarray with a highly open and porous structure on a large scale. Fig. 2d and e shows the typical SEM images of the hierarchical Co₃O₄@MnO₂ core—shell arrays on Ni foam. Clearly, ultrathin MnO₂ nanosheets are uniformly deposited on the Co₃O₄ nanowire surface after complete hydrothermal reaction in KMnO₄ solution for 24 h. The uniform array structure is still well retained even after the MnO₂ nanosheets decorated on the Co₃O₄ surface. Furthermore, the SEM images and corresponding optical images of the Ni foam, Co₃O₄ nanowires on Ni foam, and Co₃O₄@MnO₂ core—shell arrays on Ni foam (see Supplementary information, SI-2) confirm the uniform coverage of Co₃O₄ and Co₃O₄@MnO₂ core—shell arrays on Ni foam. Thus, nearly all the core—shell arrays are highly accessible to electrolyte for energy storage due to the presence of convenient diffusion channels.

The detailed structural information of Co₃O₄ nanowires and the hierarchical Co₃O₄@MnO₂ core—shell nanowires was further provided by TEM at different magnifications. The TEM samples were prepared by scratching the Co₃O₄@MnO₂ nanocomposite from Ni foam, followed by dispersing them in ethanol and dropping them on the TEM copper grids. As can be seen in the TEM images of Co₃O₄ nanowires (see Supplementary information, SI-3), the slim

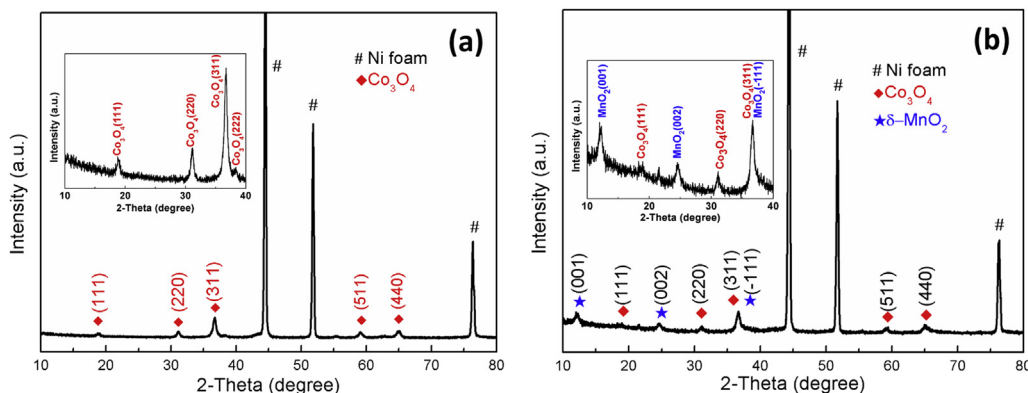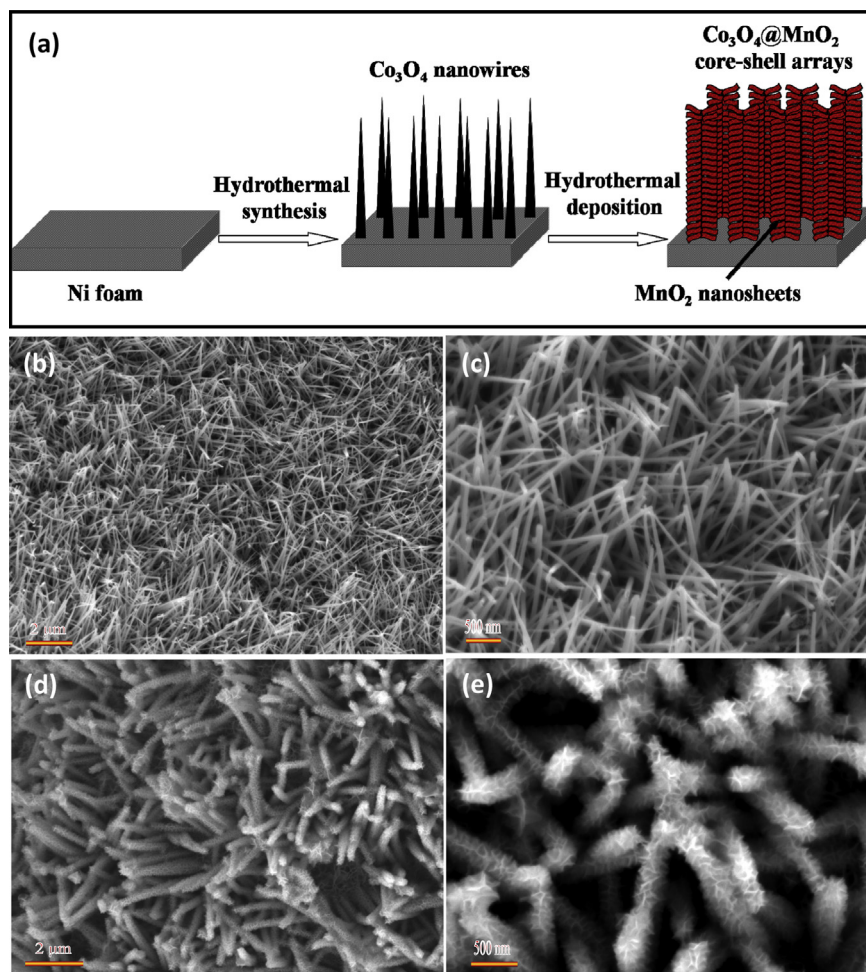**Fig. 1.** XRD patterns of Co₃O₄ nanowire arrays (a) and hierarchical Co₃O₄@MnO₂ core—shell nanowire arrays (b) on Ni foam. The insets show the magnified patterns in the range of 10—40°.

Fig. 2. (a) Schematic illustration of the two-step synthesis of hierarchical Co_3O_4@MnO_2 core–shell arrays directly on Ni foam. (b, c) Low-magnification and enlarged SEM images of the Co_3O_4 nanowires arrays on Ni foam. (d, e) Low-magnification and enlarged SEM images of the hierarchical Co_3O_4@MnO_2 core–shell nanowire arrays on Ni foam.

nanowires are highly porous, composed of nanocrystallites of 10–20 nm in size and mesopores of 5–10 nm. The clearly lattice fringes show an interplanar spacing of 0.467 nm (see Supplementary information, SI-2b), corresponding to the (111) plane of the cubic Co_3O_4. Fig. 3a and b shows the typical TEM images of the hierarchical Co_3O_4@MnO_2 core–shell nanowires obtained with 1 mmol $Co(NO_3)_2$ at different magnifications, indicating that porous Co_3O_4 nanowires were uniformly covered with small MnO_2 nanosheets. The primary MnO_2 nanosheets are ultrathin and have a thickness of ~4.5 nm, as depicted in Fig. 3c. The HRTEM image in Fig. 3c has a lattice spacing of 0.285 nm in the backbone area of the Co_3O_4 nanowire, which corresponds to the (220) interplanar spacing of

cubic Co_3O_4. The HRTEM examination of the MnO_2 shell shown in Fig. 3c reveals the interplanar spacing of 0.69 nm for two curing nanosheets, corresponding to (001) plane of birnessite-type MnO_2 [28,40–42]. The lattice distance of 0.252 nm corresponds to the (200) plane of MnO_2. These results are consistent with the previous XRD data. Furthermore, the energy-dispersive X-ray spectroscopy (EDS) (see Supplementary information, SI-4) confirms the Co_3O_4 core@MnO_2 shell hierarchical structure. The EDS line scan result for the indicated line in the core–shell structure is consistent with the EDS spectrum shown in SI-4e, in which a trace of K element is introduced into the interlayer MnO_2 during the growth [27,43] and the Cu signal comes from the Cu grid. It is worth mentioning that
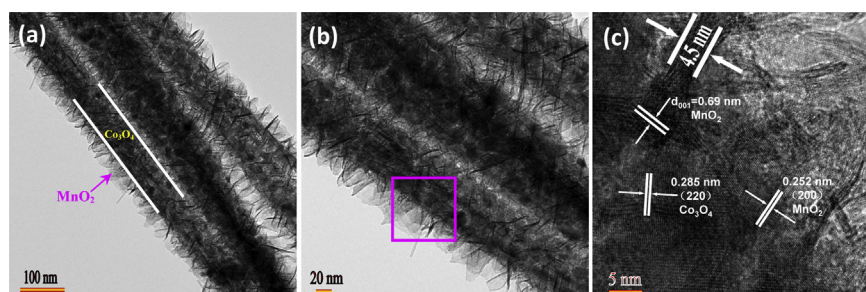
Fig. 3. (a, b) Low-magnification TEM images of the hybrid Co_3O_4@MnO_2 nanowires. (c) HRTEM image of the Co_3O_4@MnO_2 core–shell nanostructure (the boxed region in (b)).

the close contact of the MnO_2 nanosheets to the Co_3O_4 core should allow enhanced ion transport and mechanical stability.

In order to have a closer inspection of the morphologies of the hierarchical $Co_3O_4@MnO_2$ core–shell arrays, a series of mixture solution-dependent experiments were carried out. Fig. 4 presents the SEM images of the Co_3O_4 and corresponding hierarchical $Co_3O_4@MnO_2$ composite with different morphologies prepared from different mixture solution. Dense Co_3O_4 nanowires arrays and MnO_2 nanosheets decorated Co_3O_4 nanowires arrays (NWAs) can be obtained when 1.5 mmol $Co(NO_3)_2$ was used. The Co_3O_4 nanowires arrays appeared and aligned, grown with a high density on Ni foam (Fig. 4a). After MnO_2 growth, the surface of Co_3O_4 was homogeneously covered with a layer of dense MnO_2 ultrathin nanosheets as shown in Fig. 4b, resulting in a highly porous surface morphology. In another set of experiments, 2 mmol $Co(NO_3)_2$ was added, then the Co_3O_4 and $Co_3O_4@MnO_2$ nanowire@nanosheet arrays (NSWAs) were obtained (Fig. 4c and d). It demonstrates that the products exhibit urchin-like structures with multi-directional tertiary nanowires grown on the secondary nanosheets and forming a highly dense film on the major skeleton of Ni foam. Further increasing the amount of $Co(NO_3)_2$ to 4 mmol, nanowires-built clusters (NWCs) were formed with multi-directional nanowires as indicated in Fig. 4e and f. The uniform $Co_3O_4@MnO_2$ core–shell arrays on Ni foam become more compact and aggregated than the previous structures. In this procedure, we found that the morphologies of Co_3O_4 and $Co_3O_4@MnO_2$ core–shell nanocomposite can be tuned by simply adjusting the addition of $Co(NO_3)_2$. Noteworthy, the mass loading of active material per unit area would increase with the addition of $Co(NO_3)_2$, and this would lead to a negative effect to the electrochemical performance of the electrode.

3.2. Surface area and porosity analysis

To examine surface property of the hierarchical $Co_3O_4@MnO_2$ core–shell nanocomposite obtained with 1 mmol $Co(NO_3)_2$, we further measured Brunauer–Emmett–Teller (BET) and nitrogen adsorption–desorption. Fig. 5 presents the corresponding nitrogen adsorption–desorption isotherm and pore size distribution curve of the nanocomposite. The adsorption–desorption isotherm can be classified as type IV according to the profile of a hysteresis loop in a relative pressure (P/P_0) range of 0.5–1.0. This reveals that the as-prepared $Co_3O_4@MnO_2$ core–shell nanocomposite has a typical mesoporous structure, which is further verified from the Barrett–Joyner–Halenda (BJH) pore size distribution (PSD) data shown in Fig. 5b. Nitrogen adsorption–desorption results indicate that the hierarchical $Co_3O_4@MnO_2$ core–shell nanocomposite had a BET surface area of 147.1 $m^2\,g^{-1}$ with a pore volume of 0.41 $cm^3\,g^{-1}$. The pore size distribution obtained from the adsorption branch by the
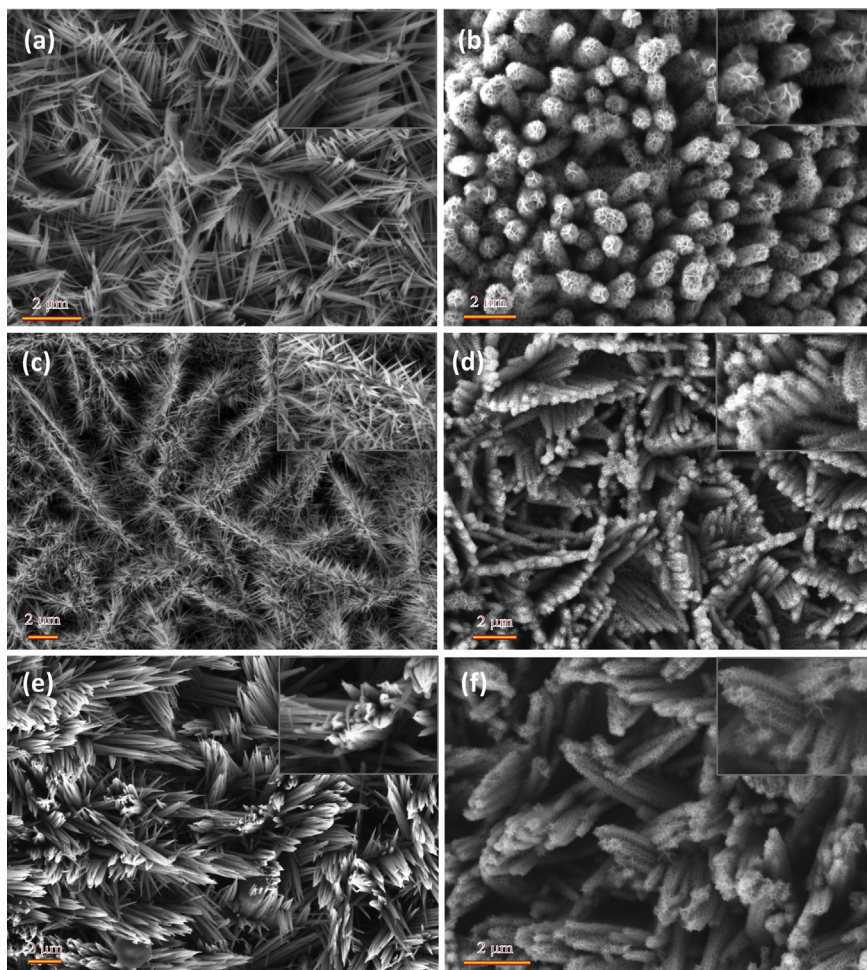
Fig. 4. SEM images of Co_3O_4 and the corresponding hierarchical $Co_3O_4@MnO_2$ composite with different morphologies by altering the mixture solution: (a, b) nanowires arrays (NWAs) obtained with 1.5 mmol $Co(NO_3)_2$, 3 mmol NH_4F, 7.5 mmol $CO(NH_2)_2$; (c, d) nanowire@nanosheet arrays (NSWAs) obtained with 2 mmol $Co(NO_3)_2$, 4 mmol NH_4F, 10 mmol $CO(NH_2)_2$; (e, f) nanowires-built clusters (NWCs) obtained with 4 mmol $Co(NO_3)_2$, 8 mmol NH_4F, 20 mmol $CO(NH_2)_2$. The insets are the corresponding magnified SEM images. Note that the hierarchical $Co_3O_4@MnO_2$ samples were obtained with 0.015 M $KMnO_4$ solution at 160 °C.
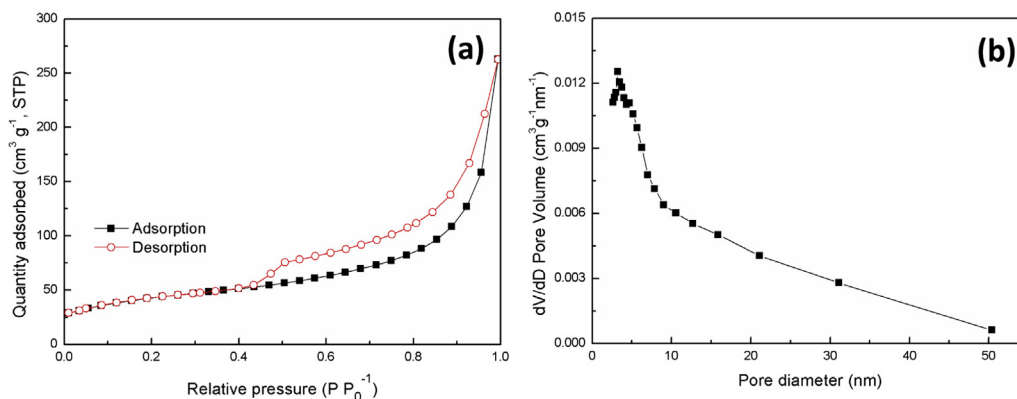
Fig. 5. Nitrogen adsorption–desorption isotherms (a) and the pore size distribution plot (b) from the adsorption branch of the hierarchical $Co_3O_4@MnO_2$ core–shell nanostructures.

Barrett–Joyner–Halenda (BJH) method indicates that the average pore size was ∼11.3 nm. The high BET specific surface area and the mesoporous structure can offer efficient transport for electrons and ions, leading to a high electrochemical capacity for the hierarchical $Co_3O_4@MnO_2$ nanocomposite.

3.3. Electrochemical properties

To evaluate potential application in electrochemical capacitors, the $Co_3O_4@MnO_2$ core–shell arrays on Ni foam obtained with 1 mmol $Co(NO_3)_2$ was applied to fabricate electrodes in a three-electrode configuration (Fig. 6). Fig. 6a presents the CV curves of

the $Co_3O_4@MnO_2$ electrodes in 1 M LiOH aqueous electrolyte at various scan rates. Although there are no distinct redox peaks, the shape of the CV curves deviates from the ideal rectangle, indicative of the faradic pseudocapacitive nature of the electrode. To further examine the electrochemical performances of the $Co_3O_4@MnO_2$ electrode, we perform galvanostatic constant current charge–discharge curves at various current densities with an electrochemical window of −0.2 to 0.4 V (Fig. 6b). The presence of the triangular symmetry and linear slopes with respect to the charging/discharging curves confirm again a good electrochemical performance. The specific capacitance obtained from the discharging curves is calculated to be 560 F g^{-1} at the current density of
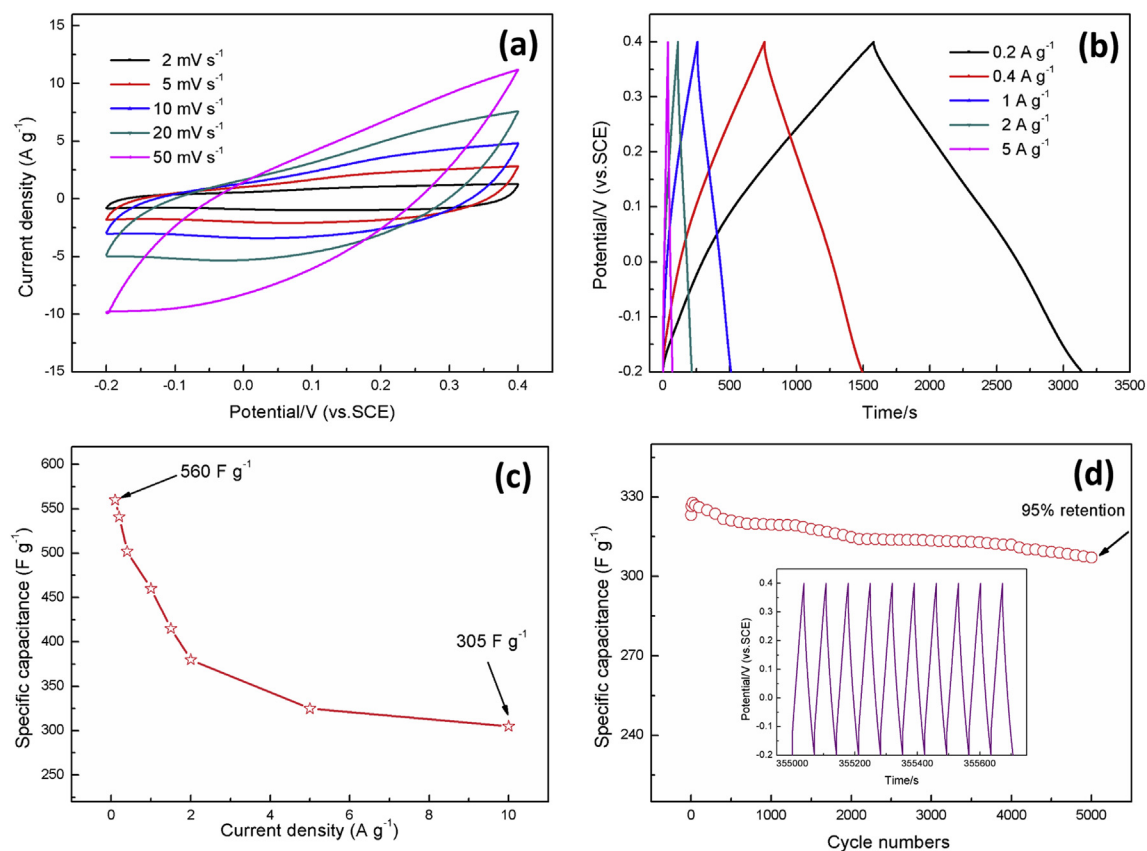
Fig. 6. (a) Cyclic voltammograms of hierarchical $Co_3O_4@MnO_2$ core–shell arrays in 1 M LiOH aqueous electrolyte. (b) Charge–discharge curves at different current densities. (c) Specific capacitance measured at different current densities. (d) Cycling performance of the electrode at the current density of 5 A g^{-1}. The inset shows the charge–discharge curves of the last 10 cycles of the $Co_3O_4@MnO_2$ electrode. Note that the hierarchical $Co_3O_4@MnO_2$ core–shell arrays were obtained with 1 mmol $Co(NO_3)_2$.

0.2 A g^{-1}, which is much higher than the pristine Co$_3$O$_4$ nanowires arrays on Ni foam (365 F g^{-1}; see Supplementary information, SI-5), indicating that the highly porous structure and the high specific surface area of the hierarchical Co$_3$O$_4$@MnO$_2$ nanostructures facilitate ion transfer to the porous structure. The electrical conductivities of pristine Ni foam, Co$_3$O$_4$ arrays on Ni foam, and Co$_3$O$_4$@MnO$_2$ core–shell arrays on Ni foam were measured by a typical four-point probe (RTS-8) technique at room temperature. The average electrical conductivities of the pristine Ni foam, Co$_3$O$_4$ arrays on Ni foam, and Co$_3$O$_4$@MnO$_2$ core–shell arrays on Ni foam were found to be 1519.8, 1049.3, and 938.1 S cm^{-1}, respectively. This means that the as-prepared Co$_3$O$_4$@MnO$_2$ core–shell arrays on Ni foam as the binder-free electrode own conductivity much better than carbon black (2–200 S cm^{-1}) [44], and the transparent carbon film electrode reported recently with a value of 206 S cm^{-1} [45]. The results indicate that the formation of the Co$_3$O$_4$@MnO$_2$ core–shell hierarchical network directly grown on Ni foam results in good electrical properties, which is beneficial for the high-performance supercapacitors. The EIS result of the Co$_3$O$_4$@MnO$_2$ core–shell hierarchical network further demonstrates that the binder-free Co$_3$O$_4$@MnO$_2$ hierarchical network directly grown on Ni foam is a favorable electrode with enhanced electrical conductivity (see Supplementary information, SI-6).

We further investigate the relationship between the specific capacitances and current densities of Co$_3$O$_4$@MnO$_2$ nanocomposite (Fig. 6c), and find that the specific capacitance decreases with the increase of the current density. The hierarchical Co$_3$O$_4$@MnO$_2$

electrode displays a moderate rate behavior, which the 54.5% of its initial capacitance is maintained when the current density increases to 10 A g^{-1}. The decrease in specific capacitance at high current densities is due to the decrease in the efficiency of utilization of the active material. We also measured the long-term cycle stability of the hierarchical Co$_3$O$_4$@MnO$_2$ nanowire arrays electrode. Fig. 6d shows cycling stability of the as-prepared hierarchical Co$_3$O$_4$@MnO$_2$ nanostructures by conducting charge–discharge tests at a current density of 5 A g^{-1} for 5000 cycles. It can be seen that the specific capacitance of Co$_3$O$_4$@MnO$_2$ electrode maintains 95% of its initial value even after 5000 cycles, indicating an excellent cycling stability of the hierarchical Co$_3$O$_4$@MnO$_2$ core–shell nanowire arrays. The charge–discharge curve of the last 10 cycles of the electrode was shown in the inset of Fig. 6d. The charge curves are still symmetric as compared to their corresponding discharge counterparts, indicating no significant structural change for the Co$_3$O$_4$@MnO$_2$ electrode during the charge–discharge processes. The charge–discharge curves obtained at the current density of 1 A g^{-1} before and after 5000 cycles (see Supplementary information, SI-7) also verify the excellent cycling stability of the hierarchical Co$_3$O$_4$@MnO$_2$ core–shell nanostructure electrode.

It is supposed that different structures might lead to different electrochemical behaviors, especially for the core–shell nanostructures assembled from nanosheets shell decorating on the nanowire core. In order to identify which structure is favorable for high performance energy storage, the hierarchical Co$_3$O$_4$@MnO$_2$ arrays with different morphologies (Co$_3$O$_4$@MnO$_2$ NWAs,
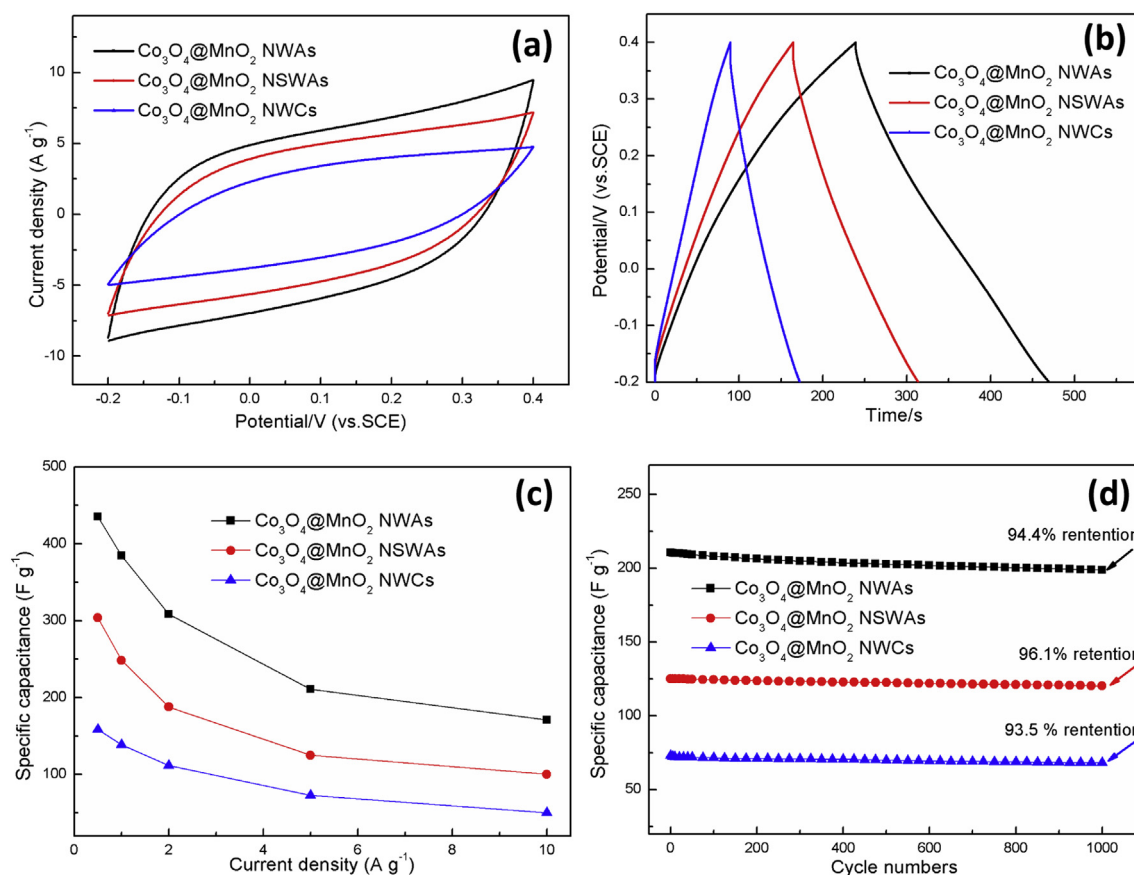

Fig. 7. (a, b) Cyclic voltammograms and charge–discharge curves of as-prepared Co$_3$O$_4$@MnO$_2$ nanowires arrays (Co$_3$O$_4$@MnO$_2$ NWAs), Co$_3$O$_4$@MnO$_2$ nanosheet@nanowire arrays (Co$_3$O$_4$@MnO$_2$ NSWAs) and Co$_3$O$_4$@MnO$_2$ nanowires-built clusters (Co$_3$O$_4$@MnO$_2$ NWCs), recorded at a scan rate of 50 mV s^{-1} and a current density of 1 A g^{-1}, respectively. (c) A comparison of specific capacitances for Co$_3$O$_4$@MnO$_2$ NWAs, Co$_3$O$_4$@MnO$_2$ NSWAs and Co$_3$O$_4$@MnO$_2$ NWCs as a function of the current densities. (d) Cycling performances of the three electrodes at the current density of 5 A g^{-1}.

NSWAs, Co$_3$O$_4$@MnO$_2$ NWCs) were used to make supercapacitors to measure their electrochemical properties in a three-electrode configuration (Fig. 7). The almost symmetric rectangular shape of the CV curves (Fig. 7a) measured at a scan rate of 50 mV s^{-1} shows reversible and capacitive behavior of the three Co$_3$O$_4$@MnO$_2$ core–shell electrodes. Obviously, the enclosed areas of the three hierarchical Co$_3$O$_4$@MnO$_2$ core–shell heterostructures are much larger than that of the corresponding pristine Co$_3$O$_4$ nanowires (see Supplementary information, SI-5a), while the enclosed area of the Co$_3$O$_4$@MnO$_2$ NWAs is the largest in the three samples, suggesting that the hierarchical heterostructures, especially the Co$_3$O$_4$@MnO$_2$ NWAs, exhibit the largest specific capacitance. Fig. 7b shows the galvanostatic constant current charge–discharge curves of the three electrodes within a potential range of −0.2 to 0.4 V, in which the charge curves are almost linear and somewhat mirror symmetrical to their discharge counterparts, suggesting good electrochemical performance for the Co$_3$O$_4$@MnO$_2$ core–shell nanostructures. The corresponding specific capacitance is 384.3, 248.5, and 138.3 F g^{-1} at a current density of 1 A g^{-1} for the Co$_3$O$_4$@MnO$_2$ NWAs, Co$_3$O$_4$@MnO$_2$ NSWAs, and Co$_3$O$_4$@MnO$_2$ NWCs, respectively, which further confirms the highest specific capacitance of the Co$_3$O$_4$@MnO$_2$ NWAs. Rate capability is a key factor for evaluating the power applications of the supercapacitors. The specific capacitances of the three samples derived from the discharging curves at different current densities are shown in Fig. 7c. It can be seen that the Co$_3$O$_4$@MnO$_2$ NWAs electrode exhibits the highest specific capacitance retention (40%) in the three samples at a high current density of 10 A g^{-1}, which is still lower

than the Co$_3$O$_4$@MnO$_2$ NWAs electrode (54.5%) obtained with 1 mmol Co(NO$_3$)$_2$. Moreover, the cycling performance tests over 1000 cycles for the three electrodes at 5 A g^{-1} were carried out using galvanostatic charge–discharge technique in the potential window of −0.2 to 0.4 V (Fig. 7d). It is noted that the three samples display good cycling stability with about 5% capacitance loss after 1000 cycles, demonstrating the good stability of the Co$_3$O$_4$@MnO$_2$ core–shell nanostructures as electrodes for supercapacitors.

To further evaluate if the hierarchical Co$_3$O$_4$@MnO$_2$ core–shell nanostructures electrode can be applied for real applications, we have fabricated an asymmetric supercapacitor using the hierarchical Co$_3$O$_4$@MnO$_2$ core–shell nanowire arrays as the positive electrode and an activated microwave exfoliated graphite oxide activated graphene (MEGO) as the negative electrode and tested it with 1 M LiOH aqueous electrolyte (see Supplementary information, SI-8a). In the design cell, the weight of Co$_3$O$_4$@MnO$_2$ core–shell structures is 0.95 mg and that of MEGO is 0.84 mg. The asymmetric device exhibits capacitive behavior with nearly rectangular-shaped CV curves without obvious redox peaks with the operating voltage up to 1.8 V (Fig. 8a). Fig. 8b shows the typical CV curves of the asymmetric cell in the voltage window from 0 to 1.6 V at the scan rates of 5, 10, 20, 50, 100, and 200 mV s^{-1}. The CV profiles of the asymmetric cell remained relatively rectangular at a high scan rate of 200 mV s^{-1}, which demonstrates good charge–discharge properties and rate capability of the asymmetric supercapacitor. The galvanostatic charge–discharge curves at various current densities are shown in Fig. 8c, which exhibit that the potentials of the charge–discharge lines are nearly proportional to the
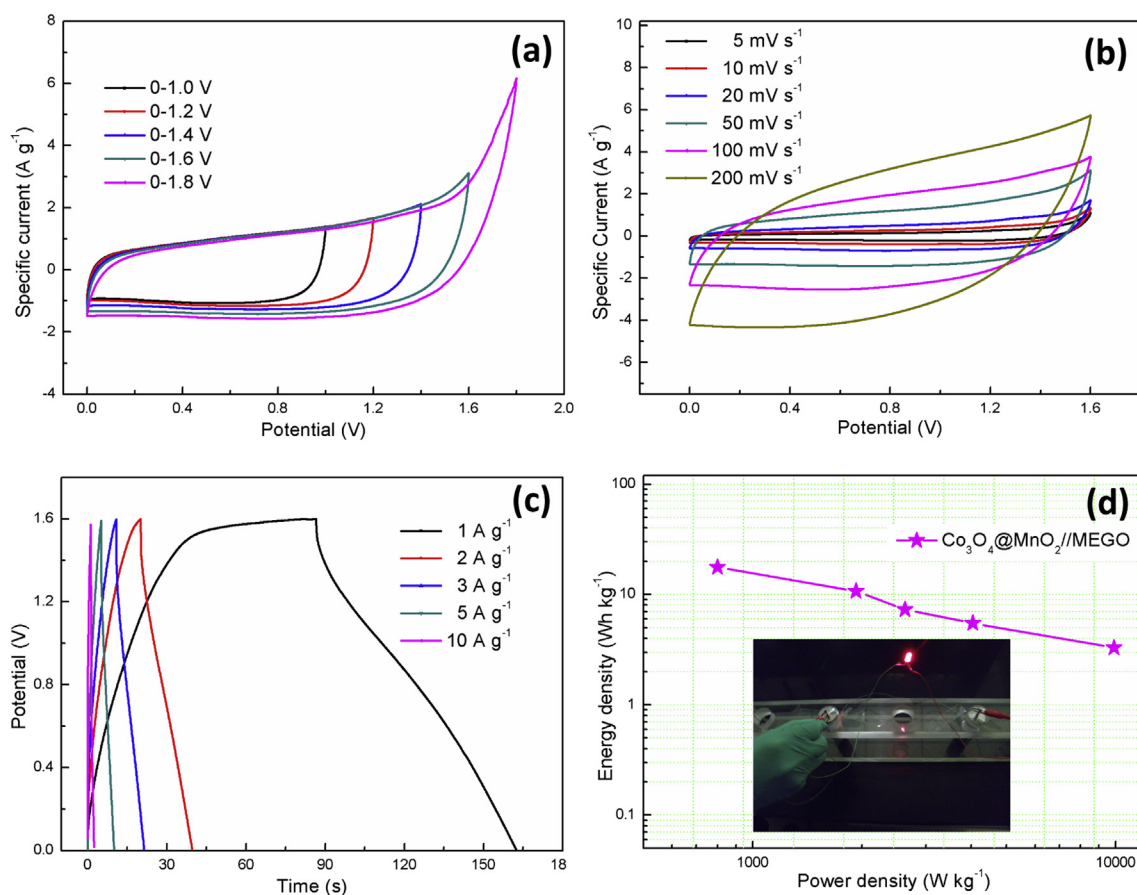
Fig. 8. (a) CV curves of Co$_3$O$_4$@MnO$_2$//MEGO asymmetric supercapacitor measured at different potential window at a scan rate of 50 mV s^{-1}. (b) CV curves of the asymmetric supercapacitor measured at different scan rates between 0 and 1.6 V. (c) Galvanostatic charge–discharge curves at different current densities. (d) Ragone plots of the asymmetric supercapacitor. The inset shows the digital image of a red-light-emitting diode (LED) lighted by the as-prepared Co$_3$O$_4$@MnO$_2$//MEGO device.

charge or discharge time, indicative of a rapid $I-V$ response, a small equivalent series resistance and an ideal capacitive characteristic, as further confirmed by the EIS data (see Supplementary information, SI-9 and Table S1). The gravimetric capacitance (Ct) of the asymmetric supercapacitor is calculated to be 49.8 F g^{-1} based on the total weight of the electrodes (i.e. mass of Co$_3$O$_4$@MnO$_2$ + MEGO) at a current density of 1 A g^{-1}. The specific capacitances of the asymmetric supercapacitor at different current densities are also investigated (see Supplementary information, SI-8b). Based on the total weight of electrodes (i.e. mass of Co$_3$O$_4$@MnO$_2$ + MEGO), we obtain a maximum gravimetric energy density of 17.7 Wh kg^{-1} and power density of 158 kW kg^{-1} (Fig. 8d). These values are much higher than those of the symmetrical supercapacitors and MnO$_2$-based asymmetric supercapacitors [39,46–51]. Thus, we connected our prototype device to a red LED and successfully lighted it (inset in Fig. 8d). In addition, we also evaluate the long-term cycle stability of the asymmetric supercapacitor at a current density of 3 A g^{-1} for 10,000 cycles. The device retained 81.1% of its initial specific capacitance after 10,000 cycles (see Supplementary information, SI-8c and SI-8d), demonstrating a minimal damage and disassembly of the electrode materials during the redox reaction. These results highlight the capability of the hierarchical Co$_3$O$_4$@MnO$_2$ core–shell nanowire arrays electrode to meet the requirements of both high specific capacitance and excellent cycling stability, which are important merits for practical energy storage devices.

4. Conclusions

In summary, we have developed a facile and cost-effective strategy to fabricate hierarchical Co$_3$O$_4$@MnO$_2$ core–shell array architectures with high electrochemical performance for supercapacitors. Owing to the synergistic effect of the mesoporous Co$_3$O$_4$ nanowires core and the ultrathin MnO$_2$ nanosheets shell, the resulting Co$_3$O$_4$@MnO$_2$ core–shell nanocomposite electrode enables facilitated ion/electron transport and accordingly exhibits a large specific capacitance, good rate capability and excellent cycling stability. An asymmetric supercapacitor based on the hierarchical Co$_3$O$_4$@MnO$_2$ core–shell nanostructure as the positive electrode and MEGO as the negative electrode delivers an energy density of 17.7 Wh kg^{-1} and a maximum power density of 158 kW kg^{-1}. These results suggest that such Co$_3$O$_4$@MnO$_2$ core–shell nanocomposite architecture directly grown on Ni foam without any conducting media and binder is very promising for next generation high-performance supercapacitors.

Acknowledgment

Appendix A. Supplementary data

Supplementary data related to this article can be found at http://dx.doi.org/10.1016/j.jpowsour.2013.12.030.

References

[1] J.R. Miller, P. Simon, Science 321 (2008) 651–652.
[2] P. Simon, Y. Gogotsi, Nat. Mater. 7 (2008) 845–854.
[3] C. Liu, F. Li, L.-P. Ma, H.-M. Cheng, Adv. Mater. 22 (2010) E28–E62.
[4] L.L. Zhang, X.S. Zhao, Chem. Soc. Rev. 38 (2009) 2520–2531.
[5] G. Wang, L. Zhang, J. Zhang, Chem. Soc. Rev. 41 (2012) 797–828.
[6] W. Wei, X. Cui, W. Chen, D.G. Ivey, Chem. Soc. Rev. 40 (2011) 1697–1721.
[7] W. Chen, R.B. Rakhi, L. Hu, X. Xie, Y. Cui, H.N. Alshareef, Nano Lett. 11 (2011) 5165–5172.
[8] W. Zhou, X. Cao, Z. Zeng, W. Shi, Y. Zhu, Q. Yan, H. Liu, J. Wang, H. Zhang, Energy Environ. Sci. 6 (2013) 2216–2221.
[9] P. Yang, X. Xiao, Y. Li, Y. Ding, P. Qiang, X. Tan, W. Mai, Z. Lin, W. Wu, T. Li, H. Jin, P. Liu, J. Zhou, C.P. Wong, Z.L. Wang, ACS Nano 7 (2013) 2617–2626.
[10] Y. Liu, D. Yan, R. Zhuo, S. Li, Z. Wu, J. Wang, P. Ren, P. Yan, Z. Geng, J. Power Sources 242 (2013) 78–85.
[11] Y. Zhang, C. Sun, P. Lu, K. Li, S. Song, D. Xue, CrystEngComm 14 (2012) 5892–5897.
[12] P. Lu, F. Liu, D. Xue, H. Yang, Y. Liu, Electrochim. Acta 78 (2012) 1–10.
[13] X.-H. Xia, J.-P. Tu, X.-L. Wang, C.-D. Gu, X.-B. Zhao, Chem. Commun. 47 (2011) 5786–5788.
[14] Y.Q. Zhang, X.H. Xia, J.P. Tu, Y.J. Mai, S.J. Shi, X.L. Wang, C.D. Gu, J. Power Sources 199 (2012) 413–417.
[15] X. Zhao, L. Zhang, S. Murali, M.D. Stoller, Q. Zhang, Y. Zhu, R.S. Ruoff, ACS Nano 6 (2012) 5404–5412.
[16] Z. Wang, C. Ma, H. Wang, Z. Liu, Z. Hao, J. Alloys Compd. 552 (2013) 486–491.
[17] Q. Qu, Y. Zhu, X. Gao, Y. Wu, Adv. Energy Mater. 2 (2012) 950–955.
[18] D.P. Dubal, G.S. Gund, R. Holze, C.D. Lokhande, J. Power Sources 242 (2013) 687–698.
[19] Y.X. Zhang, M. Huang, F. Li, X.L. Wang, Z.Q. Wen, J. Power Sources 246 (2014) 449–456.
[20] J. Zhao, Z. Lu, M. Shao, D. Yan, M. Wei, D.G. Evans, X. Duan, RSC Adv. 3 (2013) 1045–1049.
[21] Z. Sun, S. Firdoz, E.Y.-X. Yap, L. Li, X. Lu, Nanoscale 5 (2013) 4379–4387.
[22] Y. Hou, Y. Cheng, T. Hobson, J. Liu, Nano Lett. 10 (2010) 2727–2733.
[23] G. Wang, Q. Tang, H. Bao, X. Li, G. Wang, J. Power Sources 241 (2013) 231–238.
[24] H. Gao, F. Xiao, C.B. Ching, H. Duan, ACS Appl. Mater. Interfaces 4 (2012) 2801–2810.
[25] Z.-C. Yang, C.-H. Tang, H. Gong, X. Li, J. Wang, J. Power Sources 240 (2013) 713–720.
[26] L.-Q. Mai, F. Yang, Y.-L. Zhao, X. Xu, L. Xu, Y.-Z. Luo, Nat. Commun. 2 (2011) 381.
[27] J. Liu, J. Jiang, C. Cheng, H. Li, J. Zhang, H. Gong, H.J. Fan, Adv. Mater. 23 (2011) 2076–2081.
[28] L. Yu, G. Zhang, C. Yuan, X.W. Lou, Chem. Commun. 49 (2013) 137–139.
[29] L. Bao, J. Zang, X. Li, Nano Lett. 11 (2011) 1215–1220.
[30] W. Li, G. Li, J. Sun, R. Zou, K. Xu, Y. Sun, Z. Chen, J. Yang, J. Hu, Nanoscale 5 (2013) 2901–2908.
[31] H. Xia, D. Zhu, Z. Luo, Y. Yu, X. Shi, G. Yuan, J. Xie, Sci. Rep. 3 (2013) 2978.
[32] Y. Luo, D. Kong, J. Luo, S. Chen, D. Zhang, K. Qiu, X. Qi, H. Zhang, C.M. Li, T. Yu, RSC Adv. 3 (2013) 14413–14422.
[33] X. Lu, M. Yu, G. Wang, T. Zhai, S. Xie, Y. Ling, Y. Tong, Y. Li, Adv. Mater. 25 (2013) 267–272.
[34] D. Sarkar, G.G. Khan, A.K. Singh, K. Mandal, J. Phys. Chem. C 117 (2013) 15523–15531.
[35] J. Jiang, J.P. Liu, X.T. Huang, Y.Y. Li, R.M. Ding, X.X. Ji, Y.Y. Hu, Q.B. Chi, Z.H. Zhu, Cryst. Growth Des. 10 (2010) 70–75.
[36] M. Nakayama, T. Kanaya, J.-W. Lee, B.N. Popov, J. Power Sources 179 (2008) 361–366.
[37] H. Jiang, C. Li, T. . Sun, J. Ma, Nanoscale 4 (2012) 807–812.
[38] R. Chen, J. Yu, W. Xiao, J. Mater. Chem. A 1 (2013) 11682–11690.
[39] X. Zhang, P. Yu, H. Zhang, D. Zhang, X. Sun, Y. Ma, Electrochim. Acta 89 (2013) 523–529.
[40] L. Peng, X. Peng, B. Liu, C. Wu, Y. Xie, G. Yu, Nano Lett. 13 (2013) 2151–2157.
[41] J. Zhou, L. Yu, M. Sun, S. Yang, F. Ye, J. He, Z. Hao, Ind. Eng. Chem. Res. 52 (2013) 9586–9593.
[42] H. Xia, M. Lai, L. Lu, J. Mater. Chem. 20 (2010) 6896–6902.
[43] X.-D. Zhao, H.-M. Fan, J. Luo, J. Ding, X.-Y. Liu, B.-S. Zou, Y.-P. Feng, Adv. Funct. Mater. 21 (2011) 184–190.
[44] A. Kiraly, F. Ronkay, Polym. Compos. 34 (2013) 1195–1203.
[45] X. Wang, L. Zhi, N. Tsao, Z. Tomovic, J. Li, K. Muellen, Angew. Chem. Int. Ed. 47 (2008) 2990–2992.
[46] Y. He, W. Chen, X. Li, Z. Zhang, J. Fu, C. Zhao, E. Xie, ACS Nano 7 (2013) 174–182.
[47] L. Deng, G. Zhu, J. Wang, L. Kang, Z.-H. Liu, Z. Yang, Z. Wang, J. Power Sources 196 (2011) 10782–10787.
[48] Q. Cheng, J. Tang, J. Ma, H. Zhang, N. Shinya, L.-C. Qin, Carbon 49 (2011) 2917–2925.
[49] V. Khomenko, E. Raymundo-Pinero, E. Frackowiak, F. Beguin, Appl. Phys. A 82 (2006) 567–573.
[50] Y.-T. Wang, A.-H. Lu, H.-L. Zhang, W.-C. Li, J. Phys. Chem. C 115 (2011) 5413–5421.
[51] T. Cottineau, M. Toupin, T. Delahaye, T. Brousse, D. Belanger, Appl. Phys. A 82 (2006) 599–606.